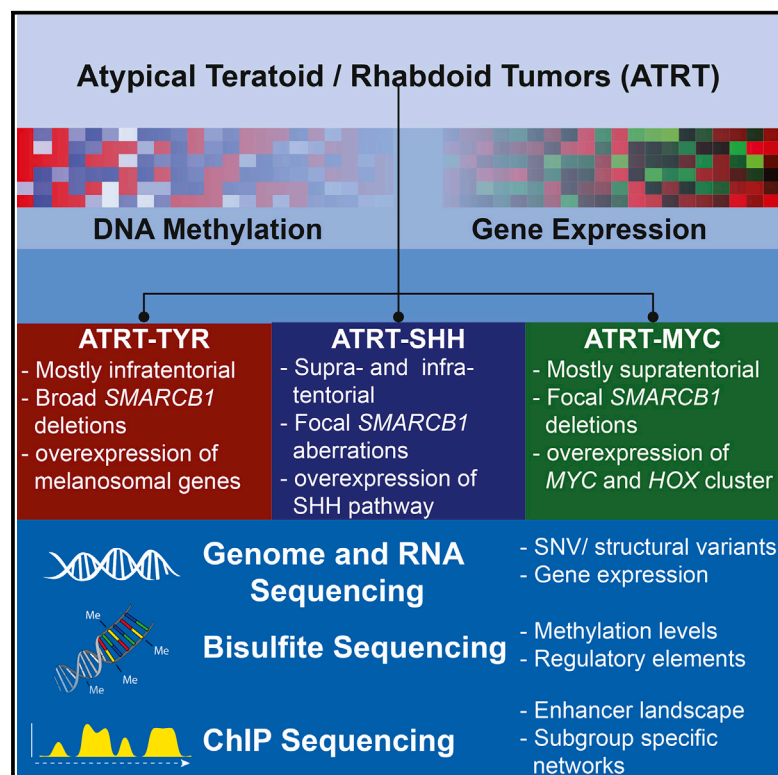# Cancer Cell

Atypical Teratoid/Rhabdoid Tumors Are Comprised of Three Epigenetic Subgroups with Distinct Enhancer Landscapes

Graphical Abstract

Authors

Pascal D. Johann, Serap Erkek, Marc Zapatka, ..., Martin Hasselblatt, Stefan M. Pfister, Marcel Kool

Correspondence

m.kool@dkfz.de

In Brief

SMARCB1 is the sole highly recurrently mutated gene in atypical teratoid/rhabdoid tumors (ATRTs). Johann et al. show that ATRTs are composed of three epigenetic subgroups that have different clinical characteristics, and identify subgroup-specific regulatory networks that suggest potential therapeutic targets.

Highlights

- ATRTs are comprised of three epigenetically distinct subgroups: TYR, SHH, and MYC

- H3K27Ac enhancer landscapes reveal ATRT subgroup-specific regulatory networks

- Regulatory networks lead to identification of potential therapeutic targets

- Epigenetic profiles point at distinct cellular origins of ATRT subgroups

Accession Numbers

GSE70460
GSE70678

CrossMark

CellPress

Atypical Teratoid/Rhabdoid Tumors Are Comprised of Three Epigenetic Subgroups with Distinct Enhancer Landscapes

Pascal D. Johann,[1,2,3,32] Serap Erkek,[1,2,4,32] Marc Zapatka,[2,5] Kornelius Kerl,[6] Ivo Buchhalter,[7] Volker Hovestadt,[2,5] David T.W. Jones,[1,2] Dominik Sturm,[1,2,3] Carl Hermann,[7] Maia Segura Wang,[4] Andrey Korshunov,[8,9] Marina Rhyzova,[10] Susanne Gröbner,[1] Sebastian Brabetz,[1] Lukas Chavez,[1] Susanne Bens,[11] Stefan Gröschel,[12] Fabian Kratochwil,[1,2] Andrea Wittmann,[1,2] Laura Sieber,[1,2] Christina Geörg,[12] Stefan Wolf,[13] Katja Beck,[2,5] Florian Oyen,[14] David Capper,[8,9] Peter van Sluis,[15] Richard Volckmann,[15] Jan Koster,[15] Rogier Versteeg,[15] Andreas von Deimling,[8,9] Till Milde,[3,16] Olaf Witt,[3,16] Andreas E. Kulozik,[3] Martin Ebinger,[17] Tarek Shalaby,[18] Michael Grotzer,[18]

(Author list continued on next page)

[1]Division of Pediatric Neurooncology, German Cancer Research Center (DKFZ), Im Neuenheimer Feld 280, Heidelberg 69120, Germany
[2]German Cancer Consortium (DKTK), Core Center Heidelberg, 69120 Heidelberg, Germany
[3]Department of Pediatric Hematology and Oncology, University Hospital Heidelberg, 69120 Heidelberg, Germany
[4]European Molecular Biology Laboratory, Genome Biology Unit, 69117 Heidelberg, Germany
[5]Division of Molecular Genetics, German Cancer Research Center, 69120 Heidelberg, Germany
[6]Department of Pediatric Hematology and Oncology, University Children's Hospital Muenster, 48149 Münster, Germany
[7]Division of Theoretical Bioinformatics, German Cancer Research Center, 69120 Heidelberg, Germany
[8]Department of Neuropathology, University Hospital Heidelberg, 69120 Heidelberg, Germany
[9]Clinical Cooperation Unit Neuropathology, German Cancer Research Center, 69120 Heidelberg, Germany
[10]Department of Neuropathology, Burdenko Neurosurgical Institute, 125047 Moscow, Russia
[11]Institute for Human Genetics, 24105 Kiel, Germany
[12]Division of Translational Oncology, Nationales Centrum für Tumorerkrankungen NCT, 69120 Heidelberg, Germany
[13]Genomics and Proteomics Core Facility, German Cancer Research Center, 69120 Heidelberg, Germany
[14]Department of Pediatric Hematology and Oncology, University Hospital Hamburg-Eppendorf, 20246 Hamburg, Germany
[15]Department of Oncogenomics, Academic Medical Center, 1105 AZ Amsterdam, the Netherlands
[16]Clinical Cooperation Unit Pediatric Oncology, German Cancer Research Center (DKFZ), 69120 Heidelberg, Germany
[17]Department of General Pediatrics, Hematology and Oncology, University of Tübingen, 72076 Tübingen, Germany
[18]Department of Neuro-Oncology, Children's Research Center, University Children's Hospital, 8032 Zürich, Switzerland

(Affiliations continued on next page)

SUMMARY

Atypical teratoid/rhabdoid tumor (ATRT) is one of the most common brain tumors in infants. Although the prognosis of ATRT patients is poor, some patients respond favorably to current treatments, suggesting molecular inter-tumor heterogeneity. To investigate this further, we genetically and epigenetically analyzed 192 ATRTs. Three distinct molecular subgroups of ATRTs, associated with differences in demographics, tumor location, and type of *SMARCB1* alterations, were identified. Whole-genome DNA and RNA sequencing found no recurrent mutations in addition to *SMARCB1* that would explain the differences between subgroups. Whole-genome bisulfite sequencing and H3K27Ac chromatin-immunoprecipitation sequencing of primary tumors, however, revealed clear differences, leading to the identification of subgroup-specific regulatory networks and potential therapeutic targets.

Significance

Our data demonstrate that ATRTs are not just one biological entity. The three molecular subgroups of ATRTs, termed ATRT-TYR, ATRT-SHH, and ATRT-MYC, are genetically similar but epigenetically very different. Whether this molecular heterogeneity may also explain the differences seen in response to current treatments needs to be validated in clinically well-annotated and similarly treated ATRT cohorts within clinical trials. The identification of molecular subgroups, (super-)enhancers, subgroup-specific regulatory networks and pathways, including potential therapeutic targets like MITF, will help to develop more effective, subgroup-specific, treatment options, which are urgently needed for this often still fatal disease. Finally, the different epigenetic profiles may also give a better insight into the potentially different cellular origin(s) of ATRTs.

David Sumerauer,[19] Josef Zamecnik,[20] Jaume Mora,[21] Nada Jabado,[22] Michael D. Taylor,[23] Annie Huang,[23] Eleonora Aronica,[24] Anna Bertoni,[5] Bernhard Radlwimmer,[5] Torsten Pietsch,[25] Ulrich Schüller,[26] Reinhard Schneppenheim,[14] Paul A. Northcott,[1,2] Jan O. Korbel,[4] Reiner Siebert,[11] Michael C. Frühwald,[27,28] Peter Lichter,[2,5,29] Roland Eils,[7,29] Amar Gajjar,[30] Martin Hasselblatt,[31] Stefan M. Pfister,[1,2,3,33] and Marcel Kool[1,2,33,*]

[19]Department of Pediatric Hematology and Oncology, Charles University and University Hospital Motol, 15006 Prague, Czech Republic
[20]Deptartment of Pathology and Molecular Medicine, Charles University, 2nd Medical Faculty, University Hospital Motol, 15006 Prague, Czech Republic
[21]Department of Hematology and Oncology, Children's Hospital, Hospital San Joan de Deu, 08950 Barcelona, Spain
[22]Departments of Pediatrics and Human Genetics, McGill University Health Center Research Institute, Montreal, QC H3A 1A4, Canada
[23]Arthur and Sonia Labatt Brain Tumor Research Centre, Hospital for Sick Children, University of Toronto, Toronto, ON M5G0A4, Canada
[24]Department of Neuropathology, Academic Medical Center, 20246 Amsterdam, the Netherlands
[25]Department of Neuropathology, University of Bonn, 53127 Bonn, Germany
[26]Center of Neuropathology, Ludwig-Maximilians-Universität, 81377 Munich, Germany
[27]Swabian Childrens' Cancer Center, Children's Hospital Augsburg, 86156 Augsburg, Germany
[28]EU-RHAB registry Center, 86156 Augsburg, Germany
[29]Heidelberg Center for Personalized Oncology, DKFZ-HIPO, DKFZ, 69120 Heidelberg, Germany
[30]St Jude Children's Research Hospital, Memphis, TN 38105, USA
[31]Institute of Neuropathology, University Hospital Münster, 48149 Münster, Germany
[32]Co-first author
[33]Co-senior author
*Correspondence: m.kool@dkfz.de
http://dx.doi.org/10.1016/j.ccell.2016.02.001

INTRODUCTION

Atypical teratoid/rhabdoid tumors (ATRTs) are among the most common aggressive brain tumors in infants (Ginn and Gajjar, 2012). Approximately 70% of all cases arise in children younger than 1 year of age and over 90% of cases occur before 3 years of age. The genetic hallmark of ATRTs are mutations in *SMARCB1*, present in the vast majority of cases (Biegel et al., 1999; Versteege et al., 1998), and frequently already present in the germline as part of a predisposition syndrome (Sredni and Tomita, 2015). Biallelic mutations of *SMARCB1* in the tumors result in complete abrogation of the SMARCB1 protein, which is assessed by immunohistochemistry in routine clinical practice and serves as a specific diagnostic marker. Rare cases that lack *SMARCB1* mutations and retain SMARCB1 protein harbor mutations in *SMARCA4* (Hasselblatt et al., 2014). Both SMARCB1 and SMARCA4 are essential components of the ATP-dependent chromatin remodeling SWI/SNF complex, which is important for lineage specification, maintenance of stem cell pluripotency, and gene regulation (Wilson and Roberts, 2011).

ATRTs were first described in the 1980s (Biggs et al., 1987) but were recognized as a separate tumor entity by the World Health Organization only in 1993 (Kleihues et al., 1993). They occur both in supratentorial and infratentorial regions of the brain. Infratentorial tumors located in the cerebellar hemispheres, cerebellopontine angle, or brain stem are more frequent in the first 2 years of life (Louis et al., 2007; Rorke et al., 1996). Overall survival of ATRT patients is poor with median survival around 17 months (Ginn and Gajjar, 2012). Treatment of ATRTs depends on the location of the tumor, initial staging, and age of the patient. While a multimodal approach combining maximal safe surgery, craniospinal irradiation (CSI), and intensive chemotherapy is considered optimal for long-term cure, the young age of many patients and involvement of critical structures within the CNS limits the use of this approach. Gross total resection is for instance impossible in a large number of patients, and CSI, although an effective component of therapy, is avoided in infants due to severe long-term neurocognitive and neuroendocrine sequelae (Squire et al., 2007). Despite this, advances in treatment for this disease have been realized, especially with the introduction of anthracycline-containing chemotherapy regimens, albeit with overall significant morbidity (Chi et al., 2009).

Despite the overall poor survival, long-term survival has been reported in a proportion of patients with ATRTs, but the biological basis for this clinical heterogeneity is unknown (Ginn and Gajjar, 2012; Lafay-Cousin et al., 2015; Slavc et al., 2014; Tekautz et al., 2005). Some studies of rather small tumor cohorts suggested that molecular heterogeneity may affect treatment responses (Birks et al., 2011; Torchia et al., 2015). Exome sequencing studies, however, revealed that rhabdoid tumors harbor very few, if any, recurrent genetic abnormalities apart from *SMARCB1* mutations (Kieran et al., 2012; Lee et al., 2012). This suggests either that *SMARCB1* inactivation is sufficient to initiate ATRTs or that other potentially synergistic events result from variations in the non-coding genome or from epigenetic deregulation. We therefore set out to elucidate the molecular landscape and heterogeneity of ATRTs.

RESULTS

Molecular Profiling of ATRTs Identifies Three Molecular Subgroups

To explore the inter-tumor heterogeneity of ATRTs we generated DNA methylation profiles and gene expression profiles of 192 histologically diagnosed primary ATRTs, almost all (188, 98%) characterized by loss of *SMARCB1* expression (Table S1). Four cases had retained *SMARCB1* expression, of which three cases were confirmed to have a *SMARCA4* mutation. Unsupervised hierarchical clustering of the DNA methylation data using 7,500 probes with the highest SD across the entire dataset identified three distinct molecular subgroups (Figure 1A). We termed the groups ATRT-TYR (n = 52), ATRT-SHH (n = 65), and ATRT-MYC (n = 33) for reasons explained later. Both consensus
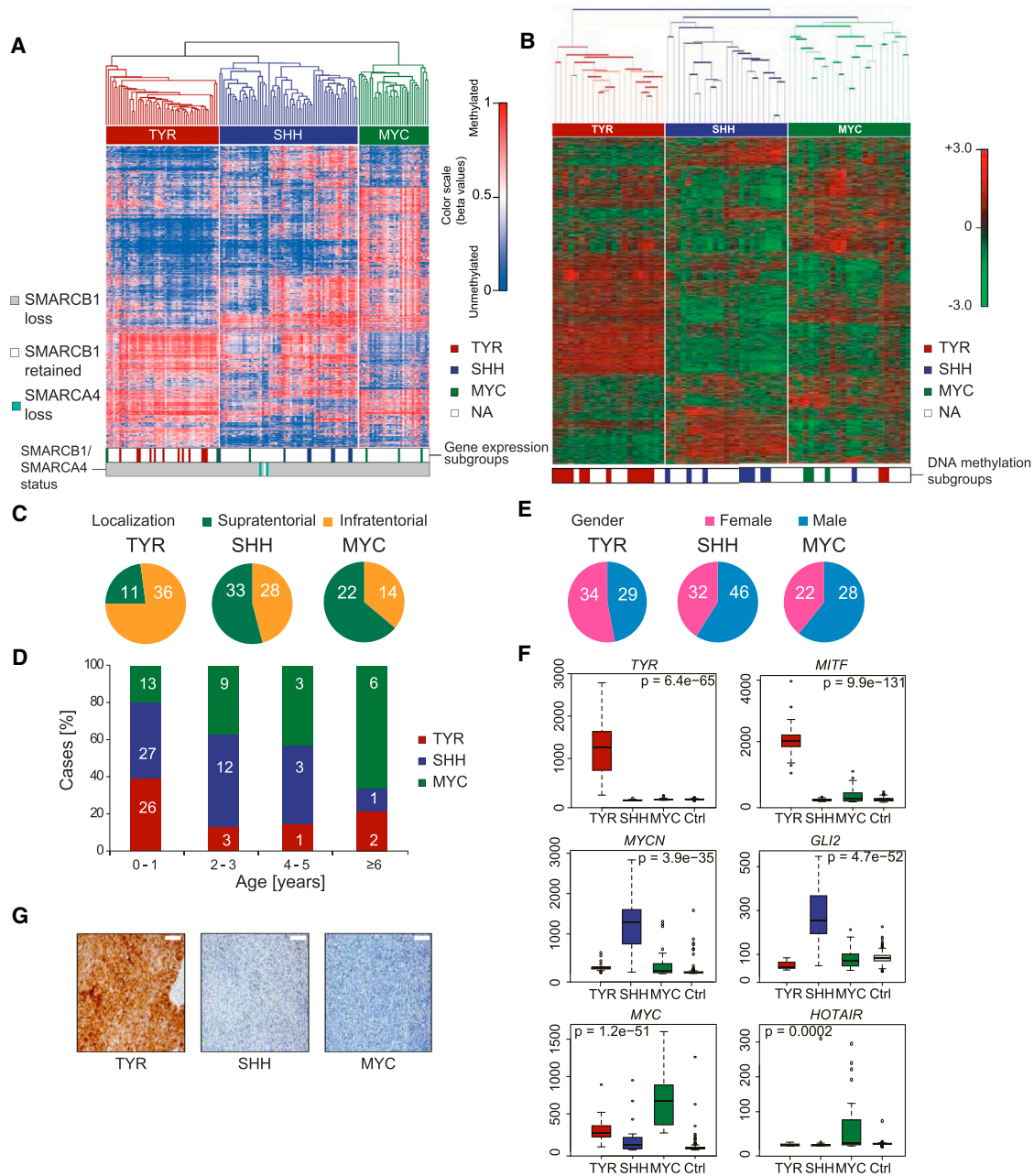
Figure 1. Unsupervised Cluster Analyses Identify Three Distinct Molecular Subgroups of ATRTs

(A) Unsupervised hierarchical clustering of 150 ATRT methylation profiles using the 7,500 most variant probes. Information on the concordance with the gene expression clustering as well as the *SMARCB1* and *SMARCA4* status is displayed in the lower bar. The level of DNA methylation (as beta value) is represented with a color scale as depicted.

(B) Unsupervised hierarchical clustering of 67 ATRT gene expression profiles using the 1,500 most differentially expressed genes. Information on the concordance with the 450k clustering is displayed in the lower bar.

(C) Pie charts showing tumor locations in the three ATRT subgroups (p = 0.00052). Absolute numbers for every localization and tumor subgroup are indicated in white.

(D) Age distributions of ATRT patients. Stacked barplots indicate frequencies and actual number of patients per age subgroup and within each ATRT subgroup.

(E) Pie charts showing gender distributions between the three ATRT subgroups (p = 0.295). Absolute numbers for both genders and tumor subgroups are indicated in white.

(F) Boxplots displaying the expression levels of representative marker genes for each of the three ATRT subgroups (boxes represent the middle 50% of data ranging from the 25% to 75% quantile a central line at the median). Whiskers represent extremes (up to 1.5-fold box size).

(G) Immunohistochemical staining for tyrosinase in one representative case from each ATRT subgroup. Scale bars denote 100 μm.

See also Figure S1 and Tables S1 and S2.

A

B

C

D

E
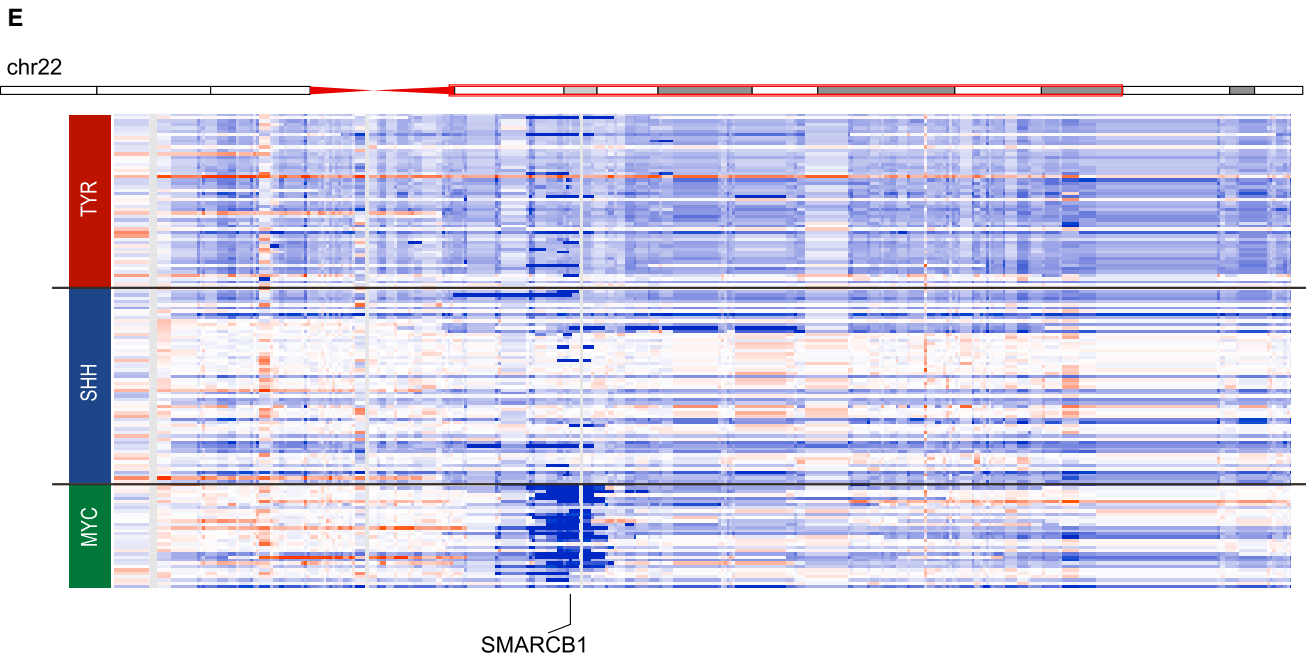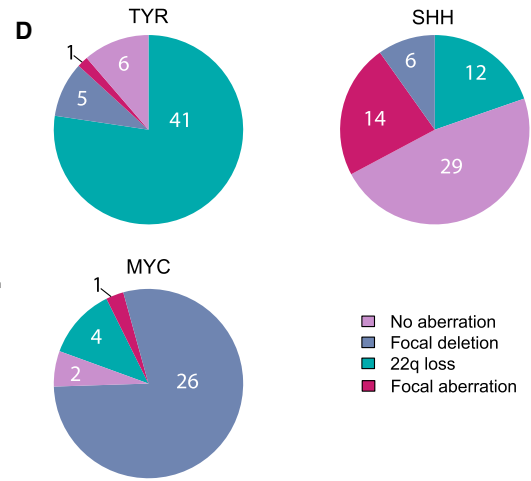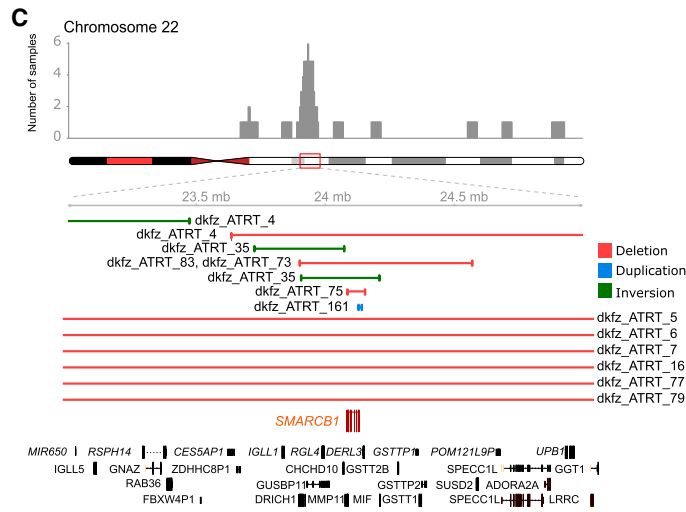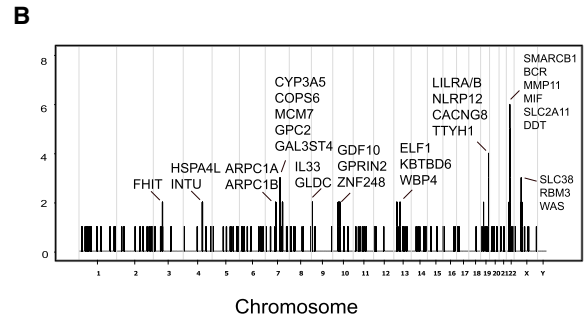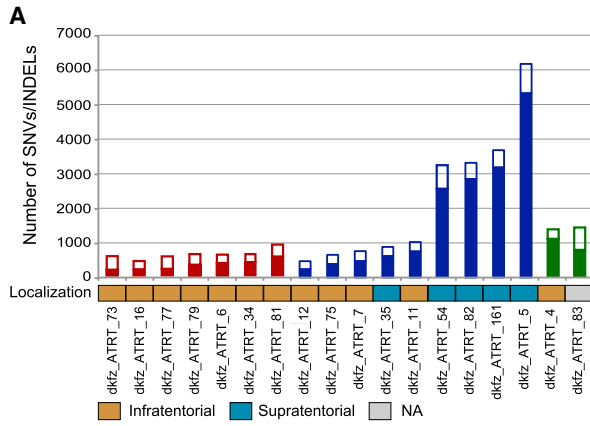
(legend on next page)

clustering and principal component analysis of the 450k DNA methylation microarray data supported the number of three distinct subgroups (Figure S1A and S1B). Three molecular subgroups were also identified when performing unsupervised hierarchical cluster analysis of gene expression profiles of 67 tumors, including 18 profiles generated by Birks et al. (2011), and including 26 cases for which we also had generated DNA methylation profiles (Figure 1B). Clustering of these cases using the 1,500 most differentially expressed genes showed a good concordance (adjusted Rand Index r = 0.88) between the two methods, with only three cases classified differently using either DNA methylation or gene expression data. All three SMARCA4 mutant cases plus the SMARCB1-positive case (presumably also SMARCA4 mutant) clustered closely together in the ATRT-SHH subgroup (Figure 1A).

In line with other brain tumor entities such as glioblastoma (Sturm et al., 2012), ATRT subgroups showed a strong enrichment for different locations in the brain. ATRT-TYR tumors were more common in infratentorial regions, while ATRT-MYC tumors mostly occurred in the supratentorial compartment. ATRT-SHH tumors located both infra- and supratentorially (Figure 1C; Table S1; p = 0.00052). Interestingly, when clustering the ATRT-SHH tumors only, three subsets were identified, of which two were associated with a supratentorial location and the third more with an infratentorial location (Figures S1C and S1D). Age at diagnosis was also different between the three molecular subgroups (Figure 1D). In the group of very young children (age 0–1 year), the TYR group was most prominently present, whereas patients in the ATRT-MYC group tended to be older. Finally, gender distributions between the subgroups did not show significant differences (Figure 1E).

Gene expression data show that ATRT-TYR tumors are characterized by overexpression of several melanosomal markers, such as MITF, TYR or DCT. TYR, encoding the enzyme tyrosinase, is highly expressed in almost every case in this subgroup, but not at all in any case of the other two subgroups (Figures 1F and 1G). TYR may therefore serve as a specific biomarker, and is the reason we propose the designation ATRT-TYR, for this molecular class. Another characteristic of this subgroup is the overexpression of many genes involved in ciliogenesis (such as DNAH11 and SPEF1) (Gene Ontology analyses, Table S2). The SHH subgroup is characterized by SHH signaling as demonstrated by high overexpression of MYCN and GLI2 (Figure 1F and Table S2). NOTCH signaling is also active in this subgroup shown by overexpression of ASCL1, HES5/6, and DLL1/3. The MYC subgroup is named after the marked overexpression of the MYC oncogene (Figure 1F) in most cases of this subgroup.

Other characteristics for the MYC subgroup include high expression of HOTAIR and many other HOX cluster genes (Figure 1F and Table S2).

Genes that are highly expressed in almost all ATRTs compared with normal brain included those encoding components of the PRC2 complex such as EZH2, SUZ12, and EED, confirming previous reports that suggest an antagonistic function of the SWI/SNF complex and PRC2 complex members and supporting the need for investigating treatment strategies that employ PRC2/EZH2 inhibition. Other drug targets overexpressed across ATRT subgroups include AURKA and HDAC1/2. In addition, VEGFA (upregulated in ATRT-TYR), CDK6 (upregulated in ATRT-SHH), and ERBB2 (upregulated in ATRT-TYR and ATRT-MYC) represent potential subgroup-specific drug targets (Figure S1E).

These results show that ATRTs are biologically heterogeneous despite sharing a loss of SMARCB1 function as the common tumorigenic event.

Whole-Genome Sequencing of ATRTs

To investigate whether other, subgroup-specific genetic aberrations not identified by exome sequencing may exist in the ATRT genome, we selected genomic DNA from 18 pairs of fresh-frozen (FF) primary ATRTs (TYR, 7; SHH, 9; MYC, 2) and corresponding blood for whole-genome sequencing (WGS) (average coverage 34×) (Tables S1 and S3). In line with the exome study (Lee et al., 2012), the overall number of coding mutations (SNVs plus indels) per sample was low (median, 7; range, 0–59) and no recurrent coding mutations besides SMARCB1 were identified except for ARMCX4, which was somatically mutated in two cases but only at low allele frequencies (Table S3). RNA sequencing was used to validate coding SNVs in samples for which we had both DNA and RNA sequencing data (SNV validation rate of 70%). The genome-wide mutation rate was also low, with a median of 508 (range 162–5,321) somatic SNVs and 299 (range 230–851) somatic indels per sample.

Four tumors from the ATRT-SHH subgroup had many more mutations than all other tumors in this series. All four had a supratentorial location (Figure 2A and Table S3). Tumors with a lower number of mutations were almost all located infratentorially. Reasons for these elevated mutation rates in these four tumors were unclear as they did not have mutations in mismatch repair genes or POLE, and mutation signatures were also not significantly different from the other tumors (data not shown).

Overall, we confirmed that ATRTs display stable genomes (Hasselblatt et al., 2013). The locus, which was most frequently affected by overlapping structural variations (SVs), was

Figure 2. WGS Confirms SMARCB1 as the Only Highly Recurrent Hit in ATRTs
(A) Barplots showing the total number of all genome-wide somatic mutations (SNVs, filled boxes; indels, open boxes) identified by WGS plotted per sample. Localization of the tumor is indicated in a panel below the barplots.
(B) Graph showing the number of samples (y axis) that have a breakpoint within a defined genomic bin (x axis). Candidate genes in these affected regions are indicated in the plot.
(C) Plot displaying different structural variations around the SMARCB1 gene identified in different ATRTs from the WGS cohort. Genes surrounding SMARCB1 are indicated in black.
(D) Pie charts showing the chromosome 22 copy number aberrations as derived from the 450k arrays. Numbers within the segments display the absolute number of cases for each category. p <2.2 × 10^{-16}.
(E) Heatmap displaying copy number profiles derived from the 450k data in a region around the SMARCB1 gene with gains (red) and losses (blue). Every row denotes one sample; subgroup assignment is indicated in the bars on the left side of the figure.
See also Figure S2 and Table S3.

SMARCB1 and neighboring genes at chromosome 22 (Figure 2B). In addition to previously described focal deletions and SNVs affecting *SMARCB1*, we found inversions and losses of the whole chromosome 22 as additional genetic events that all lead to the loss of one allele of *SMARCB1* (Figure 2C). Other loci affected by overlapping SVs, in two to four cases only, were found on chromosomes 3, 4, 7, 9, 10, 13, 19, and X (Figure 2B). However, RNA-seq analyses of 24 cases did not identify any recurrent fusion genes (data not shown).

Notably, the type of inactivating *SMARCB1* mutation as identified from the WGS cohort clearly differed between the ATRT subgroups. For instance, tumors of the ATRT-TYR subgroup mainly harbored large deletions affecting *SMARCB1* and surrounding genes on chromosome 22q, which was much less prevalent in the other two subgroups. These differences affecting chromosome 22q were validated using the larger cohort of ATRTs analyzed by 450k arrays (n = 150). We classified all copy number changes affecting chromosome 22q in this cohort as loss of chromosome 22q, focal deletions, focal aberrations (affecting only *SMARCB1*), or no detectable deletions (suggestive for *SMARCB1* missense/nonsense mutations or small indels), and again identified significant differences between the three molecular subgroups (p < 2.2 × 10^{-16}; Figures 2D, 2E, and S2). ATRT-TYR tumors indeed primarily (77%) displayed monosomy chromosome 22, which was much less prevalent in ATRT-SHH (20%) and ATRT-MYC tumors (12%). Instead, ATRT-SHH and ATRT-MYC tumors most frequently showed no chromosome 22 copy aberrations, particularly in ATRT-SHH (48%), focal gains (ATRT-SHH, 23%), or focal deletions (ATRT-MYC, 79%). These results were confirmed by multiplex ligation-dependent probe amplification (MLPA), Sanger sequencing, and fluorescence in-situ hybridization (FISH) in a subset of these tumors (n = 58, Table S1).

ATRTs Have Hypermethylated Genomes with Subgroup-Specific Differentially Methylated Regions

To investigate differences between the molecular subgroups at the epigenetic level in more detail, 17 ATRT cases (ATRT-TYR, 7; ATRT-SHH, 7; ATRT-MYC, 3) were subjected to whole-genome bisulfite sequencing (WGBS) (Table S1). Unsupervised hierarchical clustering of the WGBS data recapitulated the subgroup structure found in the array data (Figure S3A). Strikingly, a global analysis of the WGBS data revealed genome-wide hypermethylation for both ATRT-TYR and ATRT-SHH subgroups in comparison to normal cerebellum or other pediatric brain tumors like medulloblastoma, glioblastoma, or ependymoma (Bender et al., 2013; Hovestadt et al., 2014; Mack et al., 2014), with levels as high as in *IDH1*-mutated glioblastoma, which is known for its genome-wide hypermethylation (Figure 3A). CpG methylation levels in ATRT-MYC tumors were more comparable to those seen in other pediatric brain tumors. 450k array data confirmed the genome-wide hypermethylation seen in ATRT-TYR and ATRT-SHH tumors (Figure S3B).

To see whether any particular regions of the genome were relatively more hypermethylated than others, we dissected the genome into intragenic, exonic, intronic, and promoter regions (±1 kb around the transcriptional start site [TSS]) and compared methylation levels in these regions across all brain tumors and normal cerebellum. These analyses showed that hypermethyla-

tion in ATRTs was present throughout all parts of the genome, but particularly in promoter regions ATRT-TYR and ATRT-SHH cases displayed the highest differences in methylation compared with other brain tumors and normal cerebellum (Figures 3B and S3C–S3E).

The pattern of promoter hypermethylation prompted us to investigate which genes were potentially silenced by methylation. We therefore performed ANOVA statistical analyses to identify differentially methylated promoter regions when comparing ATRT subgroups with each other or with normal cerebellum controls. These analyses revealed 2,104 differentially methylated promoter regions, which we compared with the gene expression levels of the associated genes in each particular subgroup (Table S4). In total we found 369 promoters to be differentially hypermethylated in ATRT-TYR, 765 in ATRT-SHH, and 63 in ATRT-MYC. Among the respective genes we identified several tumor-suppressor genes, including *GLIPR1*, displaying strong promoter hypermethylation and downregulated in ATRT-TYR and ATRT-SHH (Figure 3C and Table S4). Methylation levels at promoters in the 450k dataset was concordant with the WGBS data and was used as a validation set (Table S4).

Several other methylation elements have been proposed to influence gene expression. For example, partially methylated domains (PMDs) are domains of disordered methylation, sometimes covering up to 30% of the total genome (Hovestadt et al., 2014). We therefore investigated whether there might be a subgroup-specific distribution of PMDs that could account for the global methylation differences seen between the ATRT subgroups. As shown in Figure 3D, PMDs were almost completely absent in ATRT-TYR cases, showed a variable distribution in ATRT-SHH cases, and were most prevalent in ATRT-MYC cases where they occupied up to 36% of the genome, partly explaining the observed global hypermethylation in ATRT-TYR and (to a lesser extent) ATRT-SHH subgroups (Figure S3F). Being linked to inactive chromatin and lamina-associated domains (Berman et al., 2012), genes inside MYC subgroup-specific PMDs showed a significantly lower expression than non-PMD genes in this subgroup. Interestingly, genes present in an ATRT-MYC subgroup-specific PMD were significantly upregulated in other subgroups when the PMD in these other subgroups was no longer hypomethylated (Figure 3E). For example, *VAV3*, a known oncogene in various cancer types (Uen et al., 2015), is located in a PMD on chromosome 1 in ATRT-MYC cases and therefore lowly expressed in tumors of this subgroup. However, in ATRT-TYR tumors where this PMD is not present, *VAV3* displayed a significantly higher expression (Figures 3F and 3G). The distinct distribution of PMDs across the subgroups thus may contribute to the different subgroup-specific transcriptomes.

DNA Methylation Valleys Are Highly Enriched for H3K27Ac and BRD4 Marks

The overall number and fraction of the genome occupied by smaller unmethylated genomic elements, such as DNA methylation valleys (DMVs) or lowly methylated regions (LMRs), did not significantly differ between the ATRT subgroups and was in general lower in the tumors than in the controls (Figures S3D and S4A). Almost all DMVs (1,392 out of 1,554, 89%) showed
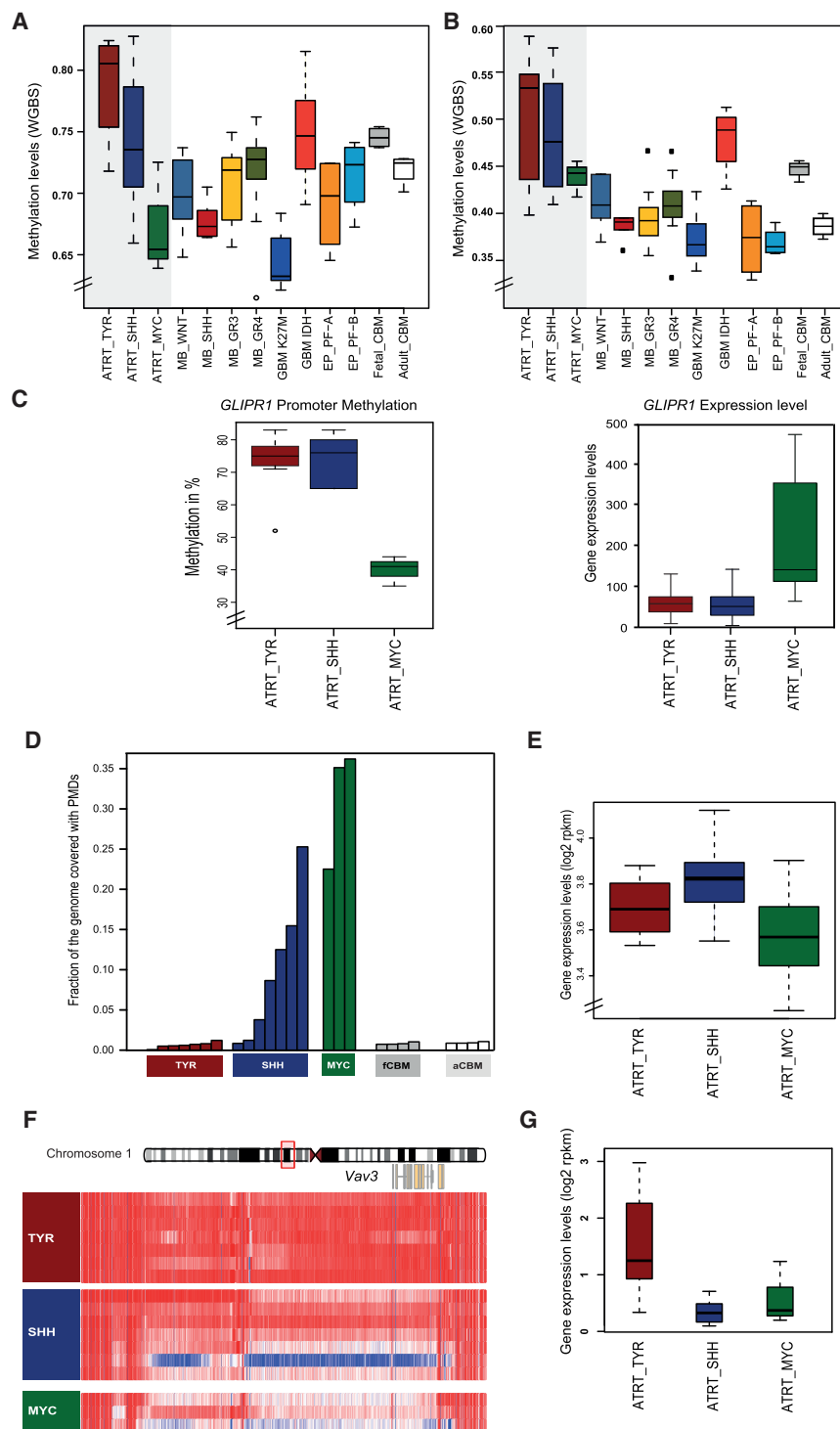
Figure 3. ATRT-TYR and ATRT-SHH Tumors Display Global Hypermethylated Genomes

(A and B) Box plots showing the mean genome-wide (A) and promoter (B) methylation levels of all CpG sides for ATRT subgroups and other molecular subgroups of pediatric brain tumors as well as normal fetal and adult cerebellum.

(C) Promoter methylation (left) and gene expression (right) of *GLIPR1* are indicated in boxplots.

(D) Barplots displaying the fraction of the genome covered by PMDs for each ATRT sample in the WGBS cohort.

(E) Mean expression level of genes that are encompassed by an ATRT-MYC-specific PMD are represented by boxplots.

(F) Metatracks displaying *VAV3*-methylation as an example for a gene covered by a PMD in all samples of the ATRT-MYC subgroup but which is hypermethylated in ATRT-TYR. Red box in the chromosome ideogram denotes the genomic region that is displayed.

(G) Box plots showing the expression of *VAV3* in the three ATRT subgroups.

Data representation by boxplots in the whole figure is the same as in Figure 1F.

See also Figure S3 and Table S4.

with active chromatin marks, we generated genome-wide ChIP-seq data for H3K27Ac and BRD4, a chromatin reader and transcriptional coactivator required for enhancer activity, for 14 primary tumor samples (ATRT-TYR, 5, ATRT-SHH, 5, ATRT-MYC, 4) for H3K27Ac (Table S1) and assessed the occupancy of DMVs and LMRs with these marks.

Across the 14 ATRT samples, we called 42,619 active enhancers (defined by the H3K27Ac peaks, but excluding those that occurred in promoter regions [± kb of TSS]). As expected, DNA methylation and H3K27Ac signals were overall strongly non-correlative (Figure 4A), while H3K27Ac and BRD4 signals were highly correlative (Figure 4B). DMVs displayed high signals for H3K27Ac, symmetrically expanding around the center of the valley. In contrast, H3K27Ac signals at LMRs were faint (Figure 4C). The same pattern was observed when analyzing the BRD4 signal at DMVs and LMRs (Figure 4C). Most DMVs overlapped with enhancers, but the average number of enhancers per sample was much higher than the average number of DMVs (Figure 4D). Overlap between LMRs and enhancers was lower (Figure 4E). *OTX2*, which encodes a brain-developmental transcription factor (TF), represents a prototypic example for the ATRT-TYR subgroup, displaying high H3K27Ac levels at a DMV in association with subgroup-specific overexpression (Figure 4F).

overlap with a gene or encompassed it completely (166 out of 1,554, 10%) (Figure S4B). Notably, the median expression levels of genes that were encompassed by a DMV was significantly higher than the genes demonstrating no overlap with a DMV (p = 2 × 10⁻²⁰, Figure S4C).

To obtain insights into whether regulatory elements characterized by lack of DNA methylation (DMVs and LMRs) are enriched
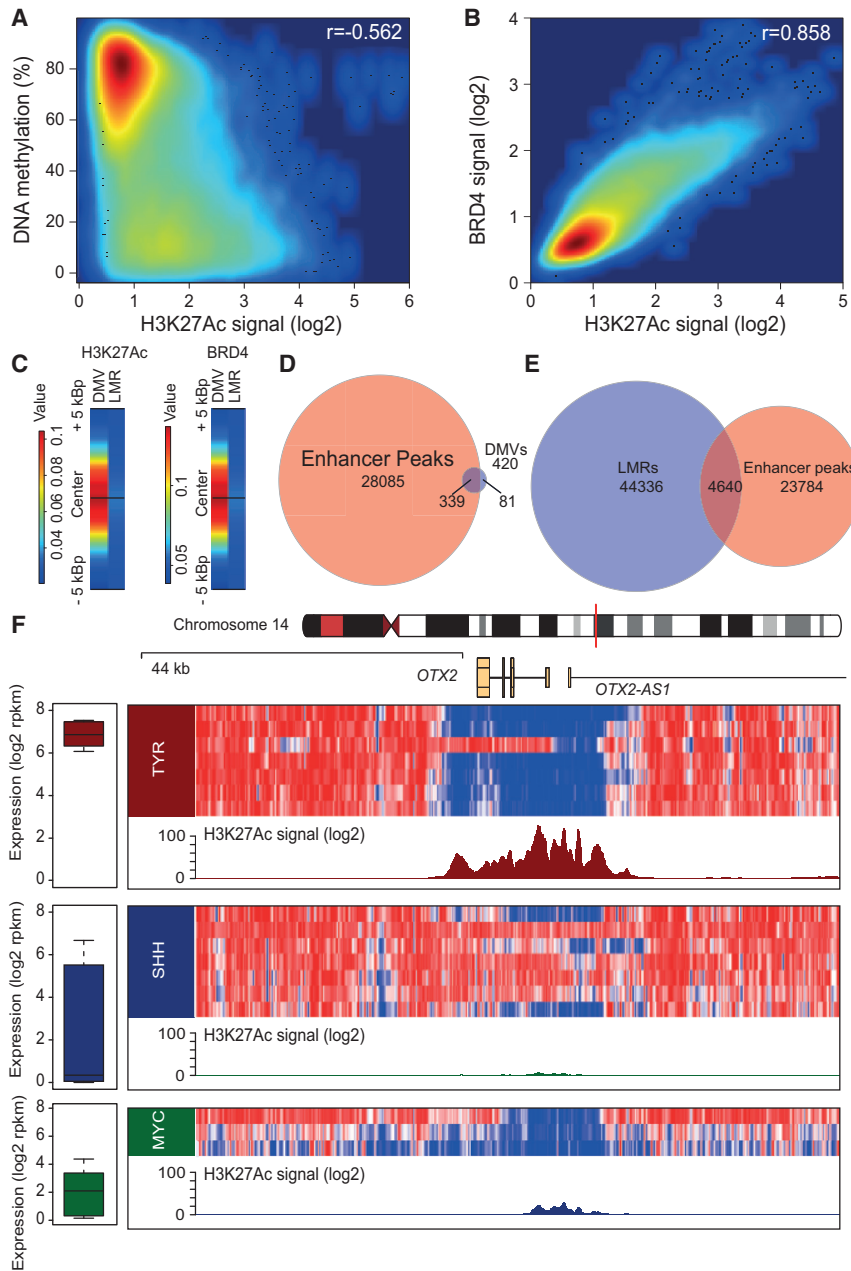
Figure 4. DNA Methylation Valleys Are Highly Enriched for the H3K27Ac Mark and BRD4 Mark

(A and B) Scatter and density plots showing the correlation between DNA methylation and H3K27Ac signals (A) and between BRD4 and H3K27Ac signals (B) at enhancers. Spearman correlation coefficients are indicated within the plots.

(C) Plots showing the relative occupancy of H3K27Ac or BRD4 in a region of ±5 kBp around the center of the DMV or LMR.

(D and E) Venn diagrams showing the overlap of DMVs (D) or LMRs (E) with H3K27Ac enhancers. Values represent the mean values for overlapping and non-overlapping DMVs or LMRs and enhancers, averaged over all samples for which H3K27Ac ChIP-seq and WGBS data were available.

(F) Metatracks of indicated subgroups showing methylation signals (heatmap at the top) and H3K27Ac signal (graph at the bottom) for a genomic region encompassing *OTX2*. Expression values for *OTX2* are indicated in boxplots on the left. Representation of the data by boxplots is the same as in Figure 1F.

See also Figure S4.

pattern in both ATRT-TYR and ATRT-SHH subgroups ("TYR_SHH high"), but was not completely absent in the ATRT-MYC subgroup (Figure 5B). The largest and most homogeneous set of specific enhancers was identified in the ATRT-TYR group (2,048 of 4,211 specific enhancers).

Assigning enhancers to the genes they regulate is not trivial, as long-distance interactions between enhancers and promoters that often span more than 50 kb may exist (Jin et al., 2013). Therefore, we addressed the question of gene-enhancer assignment using a quantitative approach by correlating H3K27Ac signals of enhancers present in one topologically associated domain (TAD; Pope et al., 2014) with expression levels of genes (as quantified by RNA sequencing) located within the same TAD. The gene whose expression best correlates with the H3K27Ac signal of one enhancer was assigned as the most probable target of the respective enhancer (see Supplemental Experimental Procedures for details). Using this approach, we were able to assign 51% of differential enhancers to their potential targets (FDR <10%) (Table S5). While the majority (66.8%) of genes was assigned to one enhancer (Figure S5A), some genes could be linked to two or more enhancers. *GLI2*, for example, highly overexpressed in ATRT-SHH, is regulated by two enhancers that are both specific for ATRT-SHH tumors (Figure 5C). Vice versa, a subset of enhancers was found to regulate more than one gene (Table S5 and Figure S5B).

A subclass of active enhancers, known as super-enhancers (SEs), is characterized by broad spatially co-localized enhancer

Subgroup-Specific Enhancers Shape Subgroup Identity of the ATRT Epigenome

From all active enhancers that we called in our H3K27Ac data, 4,899 (11.5%) were unique to ATRTs when compared with those identified in non-neoplastic tissues by others (Maher, 2012; Roadmap Epigenomics Consortium et al., 2015) (Figure 5A). Hypothesizing that the transcriptional diversity between ATRT subgroups is established by subsets of active enhancers that are specific for each subgroup, we applied ANOVA to identify these differential, active enhancers (false discovery rate [FDR] <5%, 4,211 of 42,619 enhancers, 10%). Using *k*-means clustering we discerned four distinct enhancer subclasses among these differential enhancers, corresponding to the three ATRT subgroups and one subclass of enhancers that showed a strong
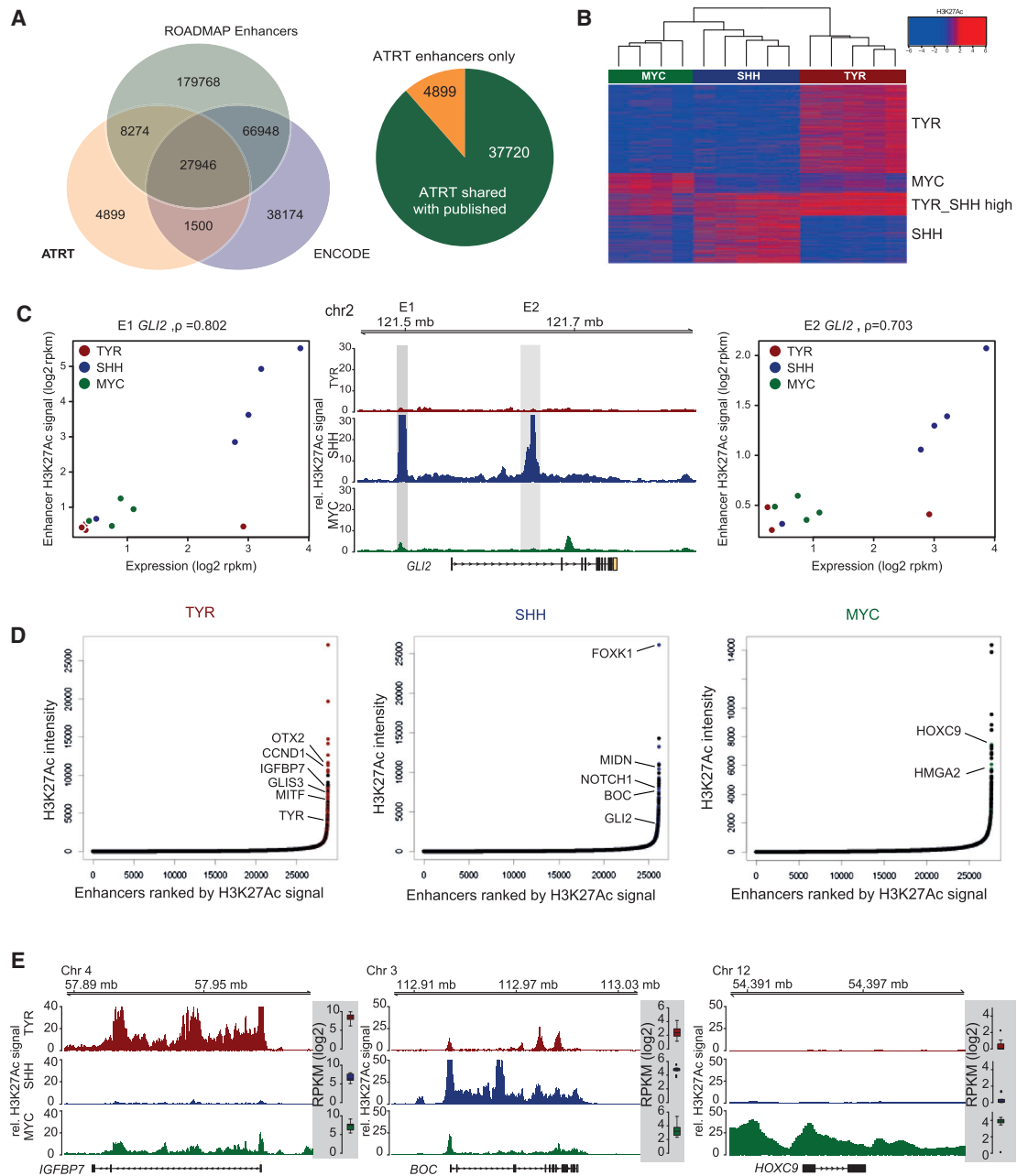
Figure 5. Subgroup-Specific (Super-)enhancers and Correlation to Gene Expression

(A) Venn-diagram showing the intersection of all ATRT enhancers with enhancers identified in ENCODE and Roadmap. The pie chart shows the fraction of identified enhancers unique to ATRT.

(B) Heatmap showing the grouping of differentially regulated enhancers (n = 4,211) into four clusters, TYR-specific (n = 2,048), MYC-specific (n = 495), TYR_SHH high (n = 542), and SHH-specific (n = 1,126) using *k*-means clustering. The H3K27Ac signal at differentially regulated enhancers is shown; 1,000 enhancers were randomly chosen for visualization purposes.

(C) Meta-track showing the H3K27Ac signal at *GLI2* in the TYR subgroup. Dot plots on both sides display the correlation between H3K27Ac signal and the enhancers regulating *GLI2* (termed E1 and E2) and the expression of *GLI2*.

(D) Plots showing enhancers ranked by increasing levels of H3K27Ac signal. Enhancers with H3K27Ac signal beyond the inflection point are qualified as SEs. Examples of SE-associated genes are highlighted on the plot for each subgroup.

(E) Metatracks displaying the H3K27Ac signal of the genes *IGFBP7*, *BOC*, and *HOXC9* associated with SEs for the respective subgroups. Boxplots to the right of the H3K27Ac plots display expression levels of the respective genes as derived from the RNA sequencing data. Data representation by boxplots in the whole figure is the same as in Figure 1F.

See also Figure S5 and Table S5.

A

B

C

D

E

F

Figure 6. TF Networks Characterizing ATRT Subgroups Converge on a Small Number of Target Molecules

(A) Heatmaps displaying the enrichment of TFs (left), and their corresponding expression values (right) across ATRT subgroups for selected TFs with highly enriched binding sites in subgroup-specific enhancers of ATRT-TYR.

(B) Plot showing the regulatory network of ATRT-TYR. Yellow/orange-colored nodes display TFs ("sources"), which show a high enrichment of their respective binding sites and differential overexpression in this subgroup. Targets of every TF are ranked and the font sizes of labels are scaled according to the degree of inward binding. Source labels are shaded according to the level of expression.

(C) Barplot showing the fraction of differentially expressed genes in ATRT-TYR for all genes, and genes that are targeted by different number of TFs (1–7).

(D) Metatracks showing the OTX2 occupancy at *MITF* and *HMGA2* loci in samples dkfz_ATRT_14 and dkfz_ATRT_16 as indicated in the plots.

(E) Heatmaps showing the scaled ChIP-seq signals for H3K27Ac (left) and OTX2 (right) at ±5 kb surrounding the midpoint of ATRT-TYR-specific enhancers. Regions are ranked by mean H3K27Ac signal (y axis).

(F) Visualization of the pathways enriched for genes regulated by ATRT-TYR subgroup-specific enhancers. Each colored point represents one enriched dataset.

See also Figure S6 and Table S6.

---

domains (Hnisz et al., 2013), and may play an essential role in establishing cell identity. SEs are established by TFs at the termini of signaling pathways (Hnisz et al., 2015). In multiple entities, SEs have been shown to drive oncogenes, genes required for maintenance of tumor cell identity, and genes associated with cell-type-specific functions.

To identify SEs in each of the ATRT subgroups, we determined and ranked the average H3K27Ac occupancy of every H3K27Ac peak across samples of a subgroup. This resulted in 894 distinct SE-containing loci, with approximately 400 SEs identified per subgroup (Table S5). Compared with typical enhancers, subgroup SEs showed higher occupancy of BRD4 and greater enhancer signal dynamic range between subgroups. Targets of differential enhancers contained within SEs (i.e., SE target genes) included several ATRT subgroup-specific signature genes like *GLI2*, *BOC*, or *NOTCH1* in subgroup ATRT-SHH (Figures 5D and 5E), and members of the melanogenesis pathway

(*MITF*, *TYR*) but also cell-cycle-related genes (e.g., *CCND1* or *IGFBP7*) in groups ATRT-TYR and ATRT-SHH (Figures 5D, 5E, S5C, and S5D). Although the number of SEs identified in ATRT-MYC was lower than in the other groups, a specific pattern of SEs could also be identified, mainly including *HOX* cluster genes such as *HOXC9* (Figures 5D and 5E). Overall, we detected a significant enrichment for TFs (p = 0.015) and cancer-related genes (p = 0.029) among the SE-regulated genes. Identification of these SE-regulated genes may thus indicate the master regulators of each ATRT subgroup.

Subgroup-Specific Regulatory Networks Converge on a Small Number of Genes

Pursuant to the idea that specific enhancers may regulate subgroup identity, we next analyzed the enrichment of transcription factor-binding sites (TFBSs) within nucleosome-free regions of subgroup-specific enhancers. These analyses identified, for each of the three molecular subgroups, a set of specific TFs whose binding motifs were significantly enriched in subgroup-specific enhancers of the respective subgroup. Interestingly, enriched TFs were also overexpressed in the respective subgroup (Figures 6A, S6A, and S6B). For example, TFBSs for OTX2 and LMX1A, both homeodomain TFs that have been implicated to

Figure 7. MITF as a Regulatory Hub in ATRT-TYR Subgroup

(A) Metatracks showing the H3K27Ac signal at *DCT*, *MITF*, and *TYR* (averaged over all samples of the respective subgroup) of the indicated subgroups. Boxplots on the right indicate the expression levels of the genes per subgroup.

(B) Barplot showing the fraction of subgroup-specific enhancers that overlap with MITF peaks. ATRT-TYR-specific enhancers show the highest identity with MITF peaks.

(C) Metatracks displaying the MITF and H3K27Ac signal around the *BMP4* locus (averaged over samples dkfz_ATRT_14 and dkfz_ATRT_16).

(D) Boxplots displaying expression of *BMP4* per subgroup as measured by the RNA-seq data.

(E) Network representing the MITF target genes. The font sizes of gene labels are scaled according to the number of ATRT-TYR-specific enhancers overlapping MITF peaks.

(legend continued on next page)

play a role in other embryonal brain tumors such as medulloblastoma, were highly enriched in the ATRT-TYR subgroup, and both factors were also highly overexpressed in this subgroup. TFBS-enrichment analysis combined with gene expression analyses for ATRT-SHH tumors further underpin a central role for SHH effectors. For instance, GLI2 is highlighted as a central TF whose binding motif is highly enriched in ATRT-SHH-specific enhancers (Figure S6A). The enrichment pattern for the ATRT-MYC subgroup is more diverse. Factors that are enriched and overexpressed in this subgroup include CEBPB and RARG (Figure S6B), but also MYC itself.

We next hypothesized that TFs identified from the TFBS-enrichment analyses may have a role in the regulation of subgroup-specific genes. We tested this by analyzing the presence of these TFBSs in subgroup-specific enhancers and inferred regulatory networks from these analyses for each molecular subgroup (Figures 6B, S6C, and S6D, Table S6). The fraction of overexpressed genes among the targets increased by the degree of inward binding, indicating that the targets which we infer are key molecules of the respective subgroup (Figures 6C, S6E, and S6F).

In order to validate the robustness of the constructed network for ATRT-TYR tumors, we performed OTX2 ChIP sequencing for two ATRT-TYR primary tumors as OTX2 was identified as master regulator in this molecular subgroup (Figure 6B). ChIP-seq data indicated that most predicted OTX2 target genes indeed displayed high occupancy with this TF, thus validating our model for the ATRT-TYR subgroup with respect to OTX2. Figure 6D shows snapshots of OTX2 binding to the *HMGA2* and the *MITF* loci, two predicted OTX2 targets in the ATRT-TYR subgroup. Data were validated by ChIP-PCR (Figure S6G). Interestingly, when examining the OTX2 occupancy at H3K27Ac peaks, we found that this TF centrally binds to specific enhancers of the TYR subgroup, thus underlining its general importance as a master regulator in the ATRT-TYR subgroup (Figure 6E).

In the networks for the TYR subgroup, *MITF* was among the three most commonly targeted genes. This gene is a well-characterized protagonist in melanoma biology, where it is frequently amplified and has been implicated in the aberrant activation of the MAP-kinase pathway (Johannessen et al., 2013). Pathway-enrichment analyses performed on the genes regulated by subgroup-specific enhancers further supported this notion (Figures 6F and S6H–S6I for the other subgroups). Aside from WNT signaling, the melanogenesis pathway was among the highly enriched pathways. This is consistent with the pathway analyses performed on our gene expression array dataset (Table S2) that highlight the melanogenesis pathway in the ATRT-TYR subgroup. We thus hypothesized that microphthalmia-associated transcription factor (MITF) may also act as a master regulator in ATRT-TYR tumors and may govern the overexpression of subgroup-specific signature genes.

MITF target genes, like *DCT* and *TYR*, have previously been examined in the context of melanoma biology. We investigated the H3K27Ac signal in the regions of *DCT* and *TYR* and found these genes to be occupied by supergroup- or subgroup-specific enhancers and differentially expressed between the ATRT subgroups (Figure 7A). Following the hypothesis that MITF targets ATRT-TYR-specific enhancers, we determined the genome-wide binding pattern of MITF in two primary samples from the ATRT-TYR subgroup by ChIP sequencing. Consistent with its role as a TF, the majority of MITF peaks were found in or near promoter regions (Figure S7A). The MITF signal expanded symmetrically around transcription start sites (Figures S7B and S7C). Strikingly, the fraction of ATRT-TYR subgroup-specific enhancers that overlapped with MITF peaks was considerably higher than with other subgroup-specific enhancers (Figure 7B). An example is *BMP4*, upregulated in subgroup ATRT-TYR, which displays a high MITF signal (Figures 7C and 7D). These data support the idea that MITF preferentially targets enhancer regions of the ATRT-TYR subgroup. The high degree of intersection between MITF peaks and subgroup-specific enhancers permitted the definition of preferential MITF targets (Figure 7E). Besides *BMP4*, *OTX2* itself was targeted by MITF, thus revealing a feedback loop between these two factors in the ATRT-TYR subgroup.

Identification of these regulatory networks and the master regulators in each of the ATRT subgroup-specific networks not only provides insight in the biology of these subgroups but may also help in identifying drug targets for subgroup-specific therapies.
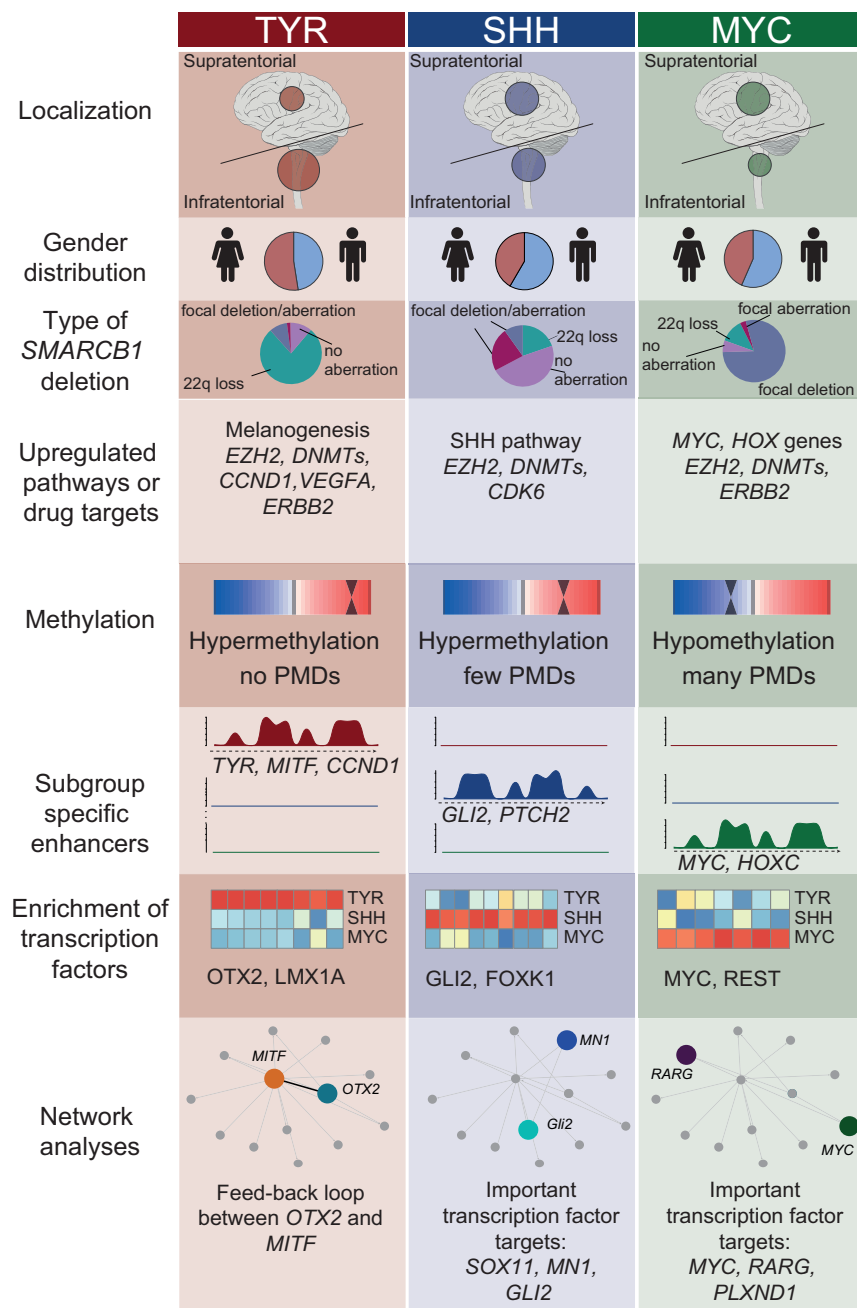
MITF Is Susceptible to In Vitro Inhibition

In melanoma, considerable efforts have been directed toward identifying drugs targeting MITF, resulting in the identification of the MITF inhibitor ML329 using a compound screen (Faloon et al., 2010). ML329 downregulates *MITF* mRNA expression and decreases cell viability in MITF-dependent melanoma cell lines. We therefore tested this compound on ATRT cell lines with low (BT16) and high (BT12) *MITF* expression (Figure S7D). Interestingly, we observed a considerable difference in the susceptibility of these cell lines toward MITF inhibition with BT12 displaying a 15-fold lower median inhibitory concentration of 460 nM (Figure 7F). This value compared favorably to MITF-dependent melanoma cell lines that have been tested in the validation runs for this compound (Faloon et al., 2010). The reduction in cell viability was found to be mainly due to an induction of apoptosis, detected by Annexin V and 7-AAD staining (Figure 7G). These results suggest that MITF inhibition could be used as a therapeutic principle to target ATRT-TYR tumors.

The epigenetic as well as demographic characteristics of the three ATRT subgroups described here are synoptically shown in Figure 8.

(F) Dose-response curve after exposure of ATRT cell lines BT12 (high *MITF* expression, red curve) and BT16 (low *MITF* expression, blue curve) to the MITF inhibitor ML329.

(G) Scatterplots displaying apoptosis rates of BT12 cells after treatment with vehicle control (1% DMSO, 72 hr; left panel) or ML329 (1 μM, 72 hr; right panel). The y axis shows the fraction of 7AAD-positive cells, the x axis indicates the Annexin V signal.

Data representation by the boxplots in this figure is the same as in Figure 1F.

See also Figure S7.

Figure 8. Synopsis on ATRT Subgroups
Overview on the three ATRT molecular subgroups and their different demographic and (epi-)genetic characteristics.

Our data show that ATRT is not a homogeneous disease even though the tumors are all characterized by the prototypic loss of expression of *SMARCB1* in the majority of cases or *SMARCA4* in the few *SMARCB1* wild-type cases. Using DNA methylation and gene expression profiling we identified three distinct molecular subgroups with different preferred locations in the brain, which suggests that they may originate from different precursor cells. Still, the cancer genomes in these three molecular subgroups are remarkably homogeneous and we did not find additional recurrent mutations from the whole-genome or RNA sequencing analyses.

Despite the few differences between the ATRT subgroups seen at a genetic level, epigenetic differences were remarkable. WGBS revealed that the ATRT-TYR subgroup, and to a lesser extent also the ATRT-SHH subgroup, but not the ATRT-MYC subgroup, were characterized by a hypermethylated genome. This can at least in part be explained by a different distribution of PMDs between the three subgroups: being almost absent in the ATRT-TYR subgroup, PMDs cover up to 36% of the genome in the ATRT-MYC subgroup. As shown by us and others in previous studies (Hovestadt et al., 2014; Lister and Ecker, 2009), these differentially methylated regions have a large impact on the expression of genes located in these PMDs, including tumor suppressors that are silenced in subgroup-specific PMDs or oncogenes that are activated in subgroups in which the PMD is not present.

The regulatory circuitries built for each of these three subgroups identified several protagonists that may represent the oncogenic drivers of a molecular subgroup. These genes may also be good targets for therapy, as we have shown for example for MITF that was identified as one of the core TFs in the ATRT-TYR subgroup.

In summary, our data provide fundamental insights into the transcriptomic and epigenomic organization of ATRTs, which will pave the way for further in vitro and in vivo studies aiming at the functional validation of therapeutic vulnerabilities. Finally, data from this study may also give hints for different cellular origin(s) of ATRTs and will form the basis for the development of mouse models recapitulating the ATRT subgroups.

DISCUSSION

Recent years have seen a surge in preclinical studies trying to identify molecular targets in ATRT. However, the vast majority of these experiments still relied on the use of cell lines, while the transcriptomic and epigenomic landscape of primary ATRT remains largely uncharted territory. Given the previously recognized differences between in vitro models and primary tumors, the use of primary material is pivotal to obtain a better understanding of the disease and to identify more effective targets for molecularly based therapies.

EXPERIMENTAL PROCEDURES

Patient Samples

Patient samples, FF or formalin-fixed paraffin-embedded (FFPE) tumor samples, and peripheral blood samples, were obtained from the EU-RHAB registry and the following single institutions: University Hospital Heidelberg, NN Burdenko Neurosurgical Institute, University of Muenster, McGill University, University of Barcelona, University of Prague, St. Judes Children's Research Hospital, University of Bonn, University of Zuerich. All tumors were banked at the time of primary diagnosis between 2009 and 2015 in accordance with research ethics board approval from the respective institutes. Informed consent was obtained from all subjects included in the study.

All samples were histologically verified ATRTs (as diagnosed by local pathologists using INI1 and SMARCA4 immunohistochemistry). DNA and RNA were isolated from the FF tumor samples, and only DNA was isolated from the FFPE tumor and blood samples using standard procedures. In a subset of tumor samples, the type of SMARCB1 mutation was characterized using MLPA, Sanger sequencing, or FISH as described above (Jackson et al., 2009). Molecular subgrouping was performed using either the 450k methylation or Affymetrix gene expression data (for subgroup information see Table S1).

Microarray Profiling

ATRT samples for which RNA of sufficient quantity and quality was available (n = 49, with 18 additional cases taken from literature) were analyzed on the Affymetrix GeneChip Human Genome U133 Plus 2.0 Array at the Microarray Department of the University of Amsterdam, the Netherlands. For details see the Supplemental Experimental Procedures. For 450k methylation array profiling, 150 ATRT samples were arrayed using the Illumina HumanMethylation450 BeadChip according to the manufacturer's instructions. Please see Supplemental Information for more details.

ACCESSION NUMBERS

Data for whole-genome DNA and RNA sequencing, whole-genome bisulfite sequencing, and ChIP sequencing for H3K27Ac, BRD4, OTX2, and MITF have been deposited at the European Genome-phenome Archive, EGA Study Accession ID EGAS00001001297. The accession number for the DNA methylation and gene expression data reported in this paper are GEO: GSE70460 and GSE70678, respectively.

SUPPLEMENTAL INFORMATION

Supplemental Information includes Supplemental Experimental Procedures, seven figures, and six tables and can be found with this article online at http://dx.doi.org/10.1016/j.ccell.2016.02.001.

AUTHOR CONTRIBUTIONS

P.D.J. and S.E. contributed equally to the manuscript. S.M.P. and M.K. conceived the study. P.D.J., S.E., S.M.P., and M.K. wrote the manuscript with input from all co-authors. P.D.J., S.E., M.Z., K.K., I.B., V.H., D.J., D.St., C.H., M.S.W., A.K., M.R., S.Gröb., S.Br., L.K., S.Be., S.Grös., F.K., A.W., L.S., C.G., S.W., K.B., F.O., D.C., P.V.S., R.Vo., J.K., R.Ve., P.A.N., P.L., J.Kor., and R.E. contributed to the design and conduct of experiments. P.D.J., S.E., M.Z., I.B., V.H., D.J., C.H., M.S.W., S.Gröb., L.K., J.K., and M.K. performed bioinformatics data analyses. A.K., M.R., D.C., A.V.D., T.P., U.S., and M.H. performed histopathological analyses of the samples. A.V.D., T.M., O.W., A.E.K., M.E., T.S., M.G., D.Su., J.Z., J.M., N.J., M.D.T., A.H., E.A., A.B., B.R., T.P., U.S., R.Sc., R.Si., M.C.F., A.G., and M.H. provided tumor samples and metadata. All authors approved the final manuscript.

ACKNOWLEDGMENTS

REFERENCES

Bender, S., Tang, Y., Lindroth, A.M., Hovestadt, V., Jones, D.T., Kool, M., Zapatka, M., Northcott, P.A., Sturm, D., Wang, W., et al. (2013). Reduced H3K27me3 and DNA hypomethylation are major drivers of gene expression in K27M mutant pediatric high-grade gliomas. Cancer Cell 24, 660–672.

Berman, B.P., Weisenberger, D.J., Aman, J.F., Hinoue, T., Ramjan, Z., Liu, Y., Noushmehr, H., Lange, C.P., van Dijk, C.M., Tollenaar, R.A., et al. (2012). Regions of focal DNA hypermethylation and long-range hypomethylation in colorectal cancer coincide with nuclear lamina-associated domains. Nat. Genet. 44, 40–46.

Biegel, J.A., Zhou, J.Y., Rorke, L.B., Stenstrom, C., Wainwright, L.M., and Fogelgren, B. (1999). Germ-line and acquired mutations of INI1 in atypical teratoid and rhabdoid tumors. Cancer Res. 59, 74–79.

Biggs, P.J., Garen, P.D., Powers, J.M., and Garvin, A.J. (1987). Malignant rhabdoid tumor of the central nervous system. Hum. Pathol. 18, 332–337.

Birks, D.K., Donson, A.M., Patel, P.R., Dunham, C., Muscat, A., Algar, E.M., Ashley, D.M., Kleinschmidt-Demasters, B.K., Vibhakar, R., Handler, M.H., and Foreman, N.K. (2011). High expression of BMP pathway genes distinguishes a subset of atypical teratoid/rhabdoid tumors associated with shorter survival. Neuro Oncol. 13, 1296–1307.

Chi, S.N., Zimmerman, M.A., Yao, X., Cohen, K.J., Burger, P., Biegel, J.A., Rorke-Adams, L.B., Fisher, M.J., Janss, A., Mazewski, C., et al. (2009). Intensive multimodality treatment for children with newly diagnosed CNS atypical teratoid rhabdoid tumor. J. Clin. Oncol. 27, 385–389.

Faloon, P.W., Bennion, M., Weiner, W.S., Smith, R.A., Wurst, J., Weiwer, M., Hartland, C., Mosher, C.M., Johnston, S., Porubsky, P., et al. (2010). A Small Molecule Inhibitor of the MITF Molecular Pathway. Probe Reports from the NIH Molecular Libraries Program (National Center for Biotechnology Information).

Ginn, K.F., and Gajjar, A. (2012). Atypical teratoid rhabdoid tumor: current therapy and future directions. Front. Oncol. 2, 114.

Hasselblatt, M., Isken, S., Linge, A., Eikmeier, K., Jeibmann, A., Oyen, F., Nagel, I., Richter, J., Bartelheim, K., Kordes, U., et al. (2013). High-resolution genomic analysis suggests the absence of recurrent genomic alterations other than SMARCB1 aberrations in atypical teratoid/rhabdoid tumors. Genes Chromosomes Cancer 52, 185–190.

Hasselblatt, M., Nagel, I., Oyen, F., Bartelheim, K., Russell, R.B., Schuller, U., Junckerstorff, R., Rosenblum, M., Alassiri, A.H., Rossi, S., et al. (2014). SMARCA4-mutated atypical teratoid/rhabdoid tumors are associated with inherited germline alterations and poor prognosis. Acta Neuropathol. 128, 453–456.

Hnisz, D., Abraham, B.J., Lee, T.I., Lau, A., Saint-Andre, V., Sigova, A.A., Hoke, H.A., and Young, R.A. (2013). Super-enhancers in the control of cell identity and disease. Cell 155, 934–947.

Hnisz, D., Schuijers, J., Lin, C.Y., Weintraub, A.S., Abraham, B.J., Lee, T.I., Bradner, J.E., and Young, R.A. (2015). Convergence of developmental and oncogenic signaling pathways at transcriptional super-enhancers. Mol. Cell 58, 362–370.

Hovestadt, V., Jones, D.T., Picelli, S., Wang, W., Kool, M., Northcott, P.A., Sultan, M., Stachurski, K., Ryzhova, M., Warnatz, H.J., et al. (2014). Decoding the regulatory landscape of medulloblastoma using DNA methylation sequencing. Nature 510, 537–541.

Jackson, E.M., Sievert, A.J., Gai, X., Hakonarson, H., Judkins, A.R., Tooke, L., Perin, J.C., Xie, H., Shaikh, T.H., and Biegel, J.A. (2009). Genomic analysis using high-density single nucleotide polymorphism-based oligonucleotide arrays and multiplex ligation-dependent probe amplification provides a comprehensive analysis of INI1/SMARCB1 in malignant rhabdoid tumors. Clin. Cancer Res. *15*, 1923–1930.

Jin, F., Li, Y., Dixon, J.R., Selvaraj, S., Ye, Z., Lee, A.Y., Yen, C.A., Schmitt, A.D., Espinoza, C.A., and Ren, B. (2013). A high-resolution map of the three-dimensional chromatin interactome in human cells. Nature *503*, 290–294.

Johannessen, C.M., Johnson, L.A., Piccioni, F., Townes, A., Frederick, D.T., Donahue, M.K., Narayan, R., Flaherty, K.T., Wargo, J.A., Root, D.E., and Garraway, L.A. (2013). A melanocyte lineage program confers resistance to MAP kinase pathway inhibition. Nature *504*, 138–142.

Kieran, M.W., Roberts, C.W., Chi, S.N., Ligon, K.L., Rich, B.E., Macconaill, L.E., Garraway, L.A., and Biegel, J.A. (2012). Absence of oncogenic canonical pathway mutations in aggressive pediatric rhabdoid tumors. Pediatr. Blood Cancer *59*, 1155–1157.

Kleihues, P., Burger, P.C., and Scheithauer, B.W. (1993). The new WHO classification of brain tumours. Brain Pathol. *3*, 255–268.

Lafay-Cousin, L., Fay-McClymont, T., Johnston, D., Fryer, C., Scheinemann, K., Fleming, A., Hukin, J., Janzen, L., Guger, S., Strother, D., et al. (2015). Neurocognitive evaluation of long term survivors of atypical teratoid rhabdoid tumors (ATRT): the Canadian registry experience. Pediatr. Blood Cancer *62*, 1265–1269.

Lee, R.S., Stewart, C., Carter, S.L., Ambrogio, L., Cibulskis, K., Sougnez, C., Lawrence, M.S., Auclair, D., Mora, J., Golub, T.R., et al. (2012). A remarkably simple genome underlies highly malignant pediatric rhabdoid cancers. J. Clin. Invest *122*, 2983–2988.

Lister, R., and Ecker, J.R. (2009). Finding the fifth base: genome-wide sequencing of cytosine methylation. Genome Res. *19*, 959–966.

Louis, D.N., Ohgaki, H., Wiestler, O.D., Cavenee, W.K., Burger, P.C., Jouvet, A., Scheithauer, B.W., and Kleihues, P. (2007). The 2007 WHO classification of tumours of the central nervous system. Acta Neuropathol. *114*, 97–109.

Mack, S.C., Witt, H., Piro, R.M., Gu, L., Zuyderduyn, S., Stutz, A.M., Wang, X., Gallo, M., Garzia, L., Zayne, K., et al. (2014). Epigenomic alterations define lethal CIMP-positive ependymomas of infancy. Nature *506*, 445–450.

Maher, B. (2012). ENCODE: the human encyclopaedia. Nature *489*, 46–48.

Pope, B.D., Ryba, T., Dileep, V., Yue, F., Wu, W., Denas, O., Vera, D.L., Wang, Y., Hansen, R.S., Canfield, T.K., et al. (2014). Topologically associating domains are stable units of replication-timing regulation. Nature *515*, 402–405.

Roadmap Epigenomics Consortium, Kundaje, A., Meuleman, W., Ernst, J., Bilenky, M., Yen, A., Heravi-Moussavi, A., Kheradpour, P., Zhang, Z., Wang, J., et al. (2015). Integrative analysis of 111 reference human epigenomes. Nature *518*, 317–330.

Rorke, L.B., Packer, R.J., and Biegel, J.A. (1996). Central nervous system atypical teratoid/rhabdoid tumors of infancy and childhood: definition of an entity. J. Neurosurg. *85*, 56–65.

Slavc, I., Chocholous, M., Leiss, U., Haberler, C., Peyrl, A., Azizi, A.A., Dieckmann, K., Woehrer, A., Peters, C., Widhalm, G., et al. (2014). Atypical teratoid rhabdoid tumor: improved long-term survival with an intensive multi-modal therapy and delayed radiotherapy. The Medical University of Vienna Experience 1992-2012. Cancer Med. *3*, 91–100.

Squire, S.E., Chan, M.D., and Marcus, K.J. (2007). Atypical teratoid/rhabdoid tumor: the controversy behind radiation therapy. J. Neurooncol. *81*, 97–111.

Sredni, S.T., and Tomita, T. (2015). Rhabdoid tumor predisposition syndrome. Pediatr. Dev. Pathol. *18*, 49–58.

Sturm, D., Witt, H., Hovestadt, V., Khuong-Quang, D.A., Jones, D.T., Konermann, C., Pfaff, E., Tonjes, M., Sill, M., Bender, S., et al. (2012). Hotspot mutations in H3F3A and IDH1 define distinct epigenetic and biological subgroups of glioblastoma. Cancer Cell *22*, 425–437.

Tekautz, T.M., Fuller, C.E., Blaney, S., Fouladi, M., Broniscer, A., Merchant, T.E., Krasin, M., Dalton, J., Hale, G., Kun, L.E., et al. (2005). Atypical teratoid/rhabdoid tumors (ATRT): improved survival in children 3 years of age and older with radiation therapy and high-dose alkylator-based chemotherapy. J. Clin. Oncol. *23*, 1491–1499.

Torchia, J., Picard, D., Lafay-Cousin, L., Hawkins, C.E., Kim, S.K., Letourneau, L., Ra, Y.S., Ho, K.C., Chan, T.S., Sin-Chan, P., et al. (2015). Molecular subgroups of atypical teratoid rhabdoid tumours in children: an integrated genomic and clinicopathological analysis. Lancet Oncol. *16*, 569–582.

Uen, Y.H., Fang, C.L., Hseu, Y.C., Shen, P.C., Yang, H.L., Wen, K.S., Hung, S.T., Wang, L.H., and Lin, K.Y. (2015). VAV3 oncogene expression in colorectal cancer: clinical aspects and functional characterization. Scientific Rep. *5*, 9360.

Versteege, I., Sevenet, N., Lange, J., Rousseau-Merck, M.F., Ambros, P., Handgretinger, R., Aurias, A., and Delattre, O. (1998). Truncating mutations of hSNF5/INI1 in aggressive paediatric cancer. Nature *394*, 203–206.

Wilson, B.G., and Roberts, C.W. (2011). SWI/SNF nucleosome remodellers and cancer. Nat. Rev. Cancer *11*, 481–492.